QUANTUM SYSTEMS

Parallel single-shot measurement and coherent control of solid-state spins below the diffraction limit

Songtao Chen*, Mouktik Raha*, Christopher M. Phenicie, Salim Ourari, Jeff D. Thompson†

Solid-state spin defects are a promising platform for quantum science and technology. The realization of larger-scale quantum systems with solid-state defects will require high-fidelity control over multiple defects with nanoscale separations, with strong spin-spin interactions for multi-qubit logic operations and the creation of entangled states. We demonstrate an optical frequency-domain multiplexing technique, allowing high-fidelity initialization and single-shot spin measurement of six rare-earth (Er^{3+}) ions, within the subwavelength volume of a single, silicon photonic crystal cavity. We also demonstrate subwavelength control over coherent spin rotations by using an optical AC Stark shift. Our approach may be scaled to large numbers of ions with arbitrarily small separation and is a step toward realizing strongly interacting atomic defect ensembles with applications to quantum information processing and fundamental studies of many-body dynamics.

A central appeal of solid-state atomic defects for quantum technology is the possibility of realizing strong dipolar interactions between closely spaced spins (*1*). This coupling enables multi-qubit logic operations [to realize, for example, error correction (*2*, *3*) or deterministic teleportation over a quantum network (*4*)] as well as fundamental studies of many-body quantum phenomena (*5*). Typically, these interactions are appreciable for defect separations less than several tens of nanometers. However, for optically addressed spins, it is an open challenge to achieve simultaneous, high-fidelity initialization, control, and readout of spins separated by less than the diffraction limit of the addressing light, typically several hundred nanometers. Several techniques have been demonstrated to simultaneously address pairs of closely spaced nitrogen vacancy centers, such as super-resolution microscopy (*6*), and variations in the Larmor frequency arising from different defect orientations (*7*, *8*) or magnetic field gradients (*9*); however, these approaches have not been extended to high-fidelity operations such as single-shot spin readout, or to larger numbers of defects. Alternatively, an array of nuclear spins surrounding a single atomic defect can be distinguished by their positions in the gradient of the hyperfine coupling (*10*–*12*); although this approach has been used to generate entanglement between as many as 10 spins (*13*), it suffers from the bottleneck that all operations are performed through a single, central electron spin.

Rare-earth ions (REIs) in solid-state hosts are a promising platform for many applications because of their demonstrated long coherence times [for example, exceeding 6 hours for Eu^{3+} (*14*)] as well as operation in the telecom band and compatibility with silicon photonics [in the case of Er^{3+} (*15*)]. Furthermore, their distinctive spectral characteristics enable frequency-domain addressing of many defects within the same spatial volume. REIs experience random, static shifts of their optical transition frequencies that give rise to an inhomogeneous (ensemble) linewidth Γ_{inh} (typically 1 to 10 GHz in crystalline hosts) that is much broader than the homogeneous linewidth of an individual ion, Γ_h (typically <1 MHz). In a given sample volume, this allows a large number of distinct subsets of ions to be separately addressed, on the order of $N_{ad} \approx \Gamma_{inh}/\Gamma_h > 10^3$. This approach can be applied to any solid-state emitter, in principle, but the especially small magnitude of Γ_{inh} and Γ_h in REIs allows the entire inhomogeneous distribution to be addressed with electro-optic sidebands on a single laser. Using spectral hole burning, this effect has been exploited in rare-earth ensembles to realize multimode atomic memories for quantum networks (*16*, *17*). Quantum gate architectures based on ensemble spectral-hole qubits have also been proposed (*18*–*21*) and demonstrated (*22*–*24*).

Frequency-domain addressing can also be used to address individual REIs within a diffraction-limited volume, if the total number of ions N is less than N_{ad}. Although detecting individual REIs is challenging (because of their low photon emission rates), this problem can be overcome by using Purcell enhancement in nanophotonic optical cavities (*15*, *25*), as exemplified by recent demonstrations of single-shot spin readout of single REIs (*26*, *27*). We combine frequency-domain addressing and high-fidelity optical control to realize initialization and single-shot spin readout of six Er^{3+} spins with submicrometer separations, coupled to a single photonic crystal cavity. Our experimental approach consists of an Er^{3+}-doped Y_2SiO_5 (YSO) crystal coupled to a silicon photonic crystal cavity (Fig. 1A). Among REIs, Er^{3+} is attractive for its telecom-wavelength optical transition and potential application to quantum networks. The cavity enhances the emission rate of the ions (*15*) and modifies the selection rules to make the optical transitions highly cyclic, enabling single-shot spin readout (*26*). The zero-field photoluminescence excitation (PLE) spectrum (Fig. 1B) shows several hundred ions within the 0.05-μm^3 mode volume of the optical cavity, with an inhomogeneous linewidth of several gigahertz. We first focus on a pair of ions located in the blue tail of the inhomogeneous distribution, labeled ion 1 and ion 2, which couple to the cavity with Purcell factors of 330 and 200, respectively, when resonant with the cavity. Because the ions are addressed through a single-mode cavity, the optical signal provides no spatial information about the ions: They are, by definition, within a single, diffraction-limited volume. Instead, the ions are addressed in the frequency domain, relying on a separation between their transitions of ~250 MHz, which is considerably larger than their linewidths (24 and 10 MHz) but smaller than the cavity linewidth of 4.2 GHz. In a magnetic field, each ion's optical transition splits into four lines that can be used to interface with its spin (Fig. 1, C and D).

First, we demonstrate simultaneous initialization and single-shot spin measurement of ion 1 and ion 2. The measurement relies on cavity-enhanced cyclicity of the optical transitions, which is controlled by the alignment of the magnetic field to the local cavity polarization (*26*). A magnetic field orientation of $[(\theta, \varphi) = (90, 150)^\circ]$ allows high cyclicity for both ions (Fig. 2A), indicating similar cavity polarization at their respective positions. We initialize the spins by optical pumping, driving the excited-state spin transition with microwaves to mix the spin levels (Fig. 2, B and C) (*27*, *28*). Then, we perform a simultaneous single-shot spin measurement by alternately exciting the spin-conserving optical transitions (A, B) on each ion. For both initialization and measurement, the laser frequency is rapidly switched between transitions by using a sideband from a fiber-coupled electro-optic modulator. We infer an initialization fidelity of ≥95%, 97% (*29*) and an average readout fidelity of 76%, 88% (Fig. 2D) for ion 1 and ion 2, respectively. The ions' spins can be coherently manipulated by using microwave pulses that address both ions equally (Fig. 2E), because the disorder in the Larmor frequency is much smaller than that of the optical transition. Details about the spin lifetime and coherence times can be found in the supplementary materials (*29*).

Next, we turn to demonstrating individually addressed spin manipulations. To achieve this, we make use of the AC Stark shift from a detuned optical pulse to induce a net phase shift ϕ between $|\uparrow\rangle$ and $|\downarrow\rangle$ (*30*). The optical pulses

Department of Electrical Engineering, Princeton University, Princeton, NJ 08544, USA
*These authors contributed equally to this work.
†Corresponding author. Email: jdthompson@princeton.edu

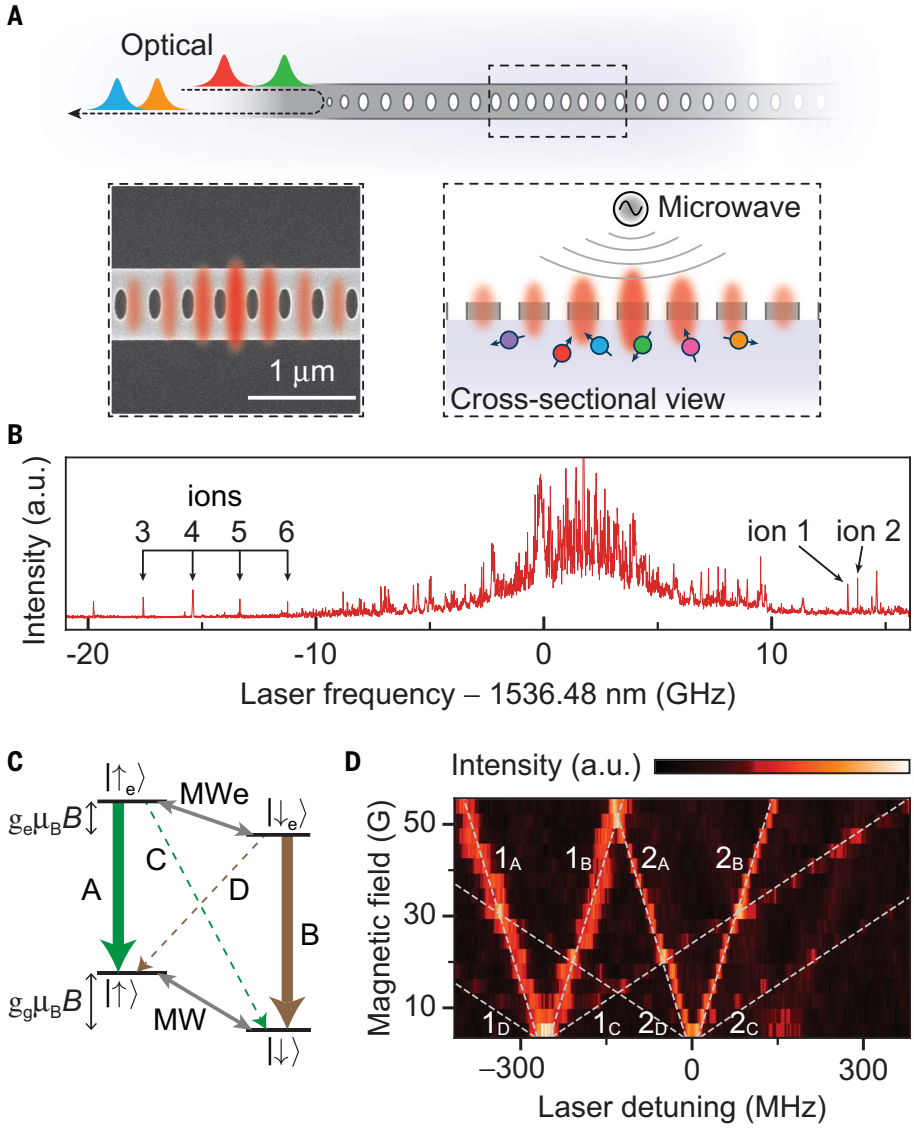

Fig. 1. Spectrally addressing multiple ions in a diffraction-limited volume. (**A**) Schematic of the device, showing multiple ions with different transition frequencies (colors) coupled to the cavity. (Inset) Scanning electron microscope image of a representative cavity, showing the extent of the optical mode. (**B**) PLE spectrum of Er^{3+} ions in a single device with magnetic field $B = 0$. Arrows indicate the six ions used in this work. (**C**) Level structure of Er^{3+}:YSO in a magnetic field, with optical (A to D) and microwave (MW, MWe) transitions indicated. g_g (g_e) denotes the ground- (excited-) state magnetic g-factor. (**D**) PLE spectrum of ion 1 and ion 2 in the presence of a magnetic field (oriented along the D_2 axis of the YSO crystal). (1_A,1_B) and (2_A,2_B) correspond to the spin-conserving optical transitions (A, B) of the two ions, respectively. Zero detuning in this panel and subsequent figures refers to the ion 2 resonance when $B = 0$. a.u., arbitrary units.

are inserted into an XY8 sequence that mitigates low-frequency magnetic field noise during the phase accumulation time. For each ion, the accumulated phase shift is $\phi = T\Omega^2(\Delta_B^{-1} - \Delta_A^{-1})/4$, where T is the pulse duration, Ω is the optical Rabi frequency, and Δ_A, Δ_B are the detunings of the laser from the spin-conserving transitions A, B (Fig. 3A, inset). For a given laser frequency and intensity, the detuning and Rabi frequency are different for each ion, enabling local control of the phase shift. To control N ions, $N-1$ laser frequencies are needed, because microwave rotations provide an additional control axis (*29*). Here, with $N = 2$, we can control both ions independently using a single laser frequency. In addition to the phase shift, there is also a loss of coherence from photon scattering and fluctuations in the optical transition frequency (e.g., from spectral diffusion), which happens at a rate $\Gamma' \propto \Gamma\Omega^2(\Delta_A^{-2} + \Delta_B^{-2})$, where Γ is the effective transition linewidth (*29*).

We measure the optically induced phase shift and decoherence using Ramsey spectroscopy, where the decoherence manifests as a change in visibility (Fig. 3A). To select the optimum operational point, we characterize the phase shift and decoherence as a function of laser frequency (Fig. 3B). The results are in good agreement with a theoretical model. The ratio of phase shift to decoherence is optimized for large detunings, and we predict a 2.55% loss of visibility per radian of differential phase shift $\Delta\phi = \phi_2 - \phi_1$ at 350 MHz detuning. In this regime, the experimental loss of visibility over a $\pi/2$ phase shift is below our measurement resolution.

In combination with a global microwave rotation $R_z(-\phi_1)$, the differential phase $\Delta\phi$ gives rise to a net rotation on ion 2 alone: $R_z^{(2)}(\Delta\phi) = \mathbb{I} \otimes R_z(\Delta\phi)$ (Fig. 3C). Similarly, a global microwave rotation $R_z(-\phi_2)$ generates a rotation on ion 1 alone. Here, $R_{\hat{n}}(\alpha)$ denotes a rotation by an angle α about axis $\hat{n}$. Universal control of a single qubit requires arbitrary angle rotations around two orthogonal axes. However, global microwave rotations can transform ion-selective optical z rotations into rotations around an arbitrary axis (*29*). As an example, we demonstrate rotations about the x axis, $R_x^{(i)}(\Delta\phi)$, where $i = 1, 2$ denotes the target ion (Fig. 3, C and D), realizing more than 2π rotation as the optical pulse duration is varied.

Lastly, we extend our approach to demonstrate simultaneous spin initialization and readout with four additional ions, labeled ion 3 to ion 6 (Fig. 1B). To access them, we shift the cavity resonance to −14.8 GHz (with respect to Fig. 1B), resulting in Purcell factors of 130, 260, 360, and 50. After choosing a magnetic field orientation that allows high cyclicity for all ions (*29*), we perform single-shot readout measurements. Because of the larger spread of these ions' frequencies (6.4 GHz) with respect to the cavity linewidth, it is advantageous to perform the readout using only one of the A or B transitions for each ion, whichever has larger Purcell enhancement (Fig. 4A). The average readout fidelities for each ion are 80, 74, 87, and 71%, respectively (Fig. 4B). The mean readout fidelity of the four-ion set is 78%, which is slightly lower than that of the two-ion set of 82%, because of the low Purcell factor of ion 6. Although the ions are measured sequentially, the total measurement duration (300 ms) is much shorter than the ground-state spin T_1 [typically > 10 s (*29*)], such that the measurements are effectively simultaneous.

In Fig. 4C, we show simultaneous microwave-driven Rabi oscillations on all four ions after initializing into $|\uparrow\uparrow\downarrow\downarrow\rangle$. Because ion 4 is situated in a crystallographic site rotated from that of the other ions, it has a different coupling to the microwave waveguide and correspondingly different Rabi frequency. In this measurement, the static field B lies in the $D_1 - D_2$ plane such that all ions have the same Larmor frequency, but we note that rotating B out of this plane

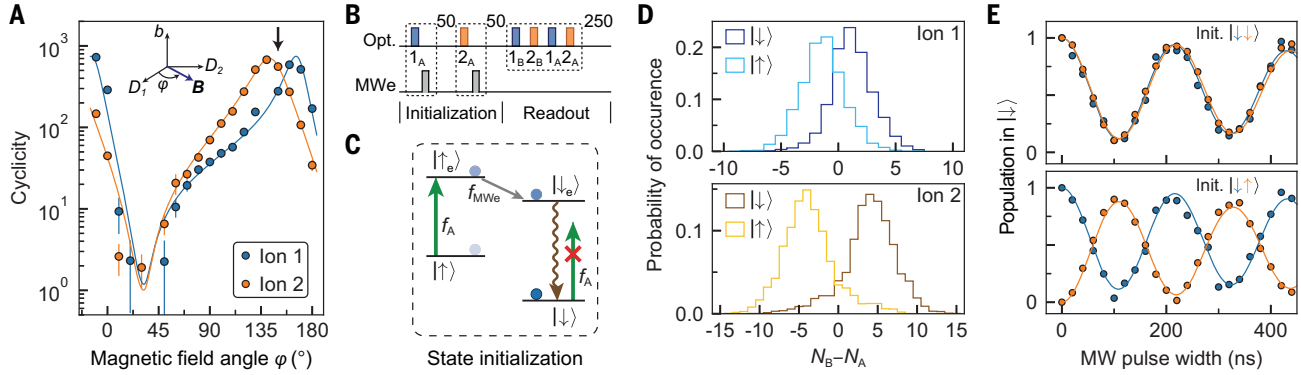

Fig. 2. Simultaneous initialization and readout of ions 1 and 2. (**A**) Cyclicity of the optical transitions (defined as $1+\ \Gamma_{A,B}/\Gamma_{C,D}$, where Γ_i is the Purcell-enhanced decay rate on transition i) as a function of magnetic field angle (see inset). The solid lines are fits to a theoretical model from (*26*), and the black arrow indicates the orientation used in subsequent experiments ($\varphi = 150°$). (**B**) Pulse scheme used for spin initialization (in this case, to $|\downarrow\rangle$) and readout. The exponents 50, 250 denote the number of repetitions of the sequence. All optical and microwave pulses are π pulses. (**C**) Diagram of the initialization sequence. A dark state emerges in $|\downarrow\rangle$ from the combination of optical excitation of the spin-conserving A transition and microwave driving of the excited-state spin. Exciting B instead will initialize the spin to $|\uparrow\rangle$. (**D**) Photon histograms showing simultaneous single-shot readout for both ions. The ions are probed alternately on their A and B transitions, and $N_B - N_A$ denotes the difference in detected counts. $N_B > N_A$ indicates that the spin state is $|\downarrow\rangle$. (**E**) Simultaneous Rabi oscillations are observed while driving the ground-state spin of both ions with a microwave pulse after initialization into the indicated states. The vertical axes are corrected for initialization and readout fidelity.

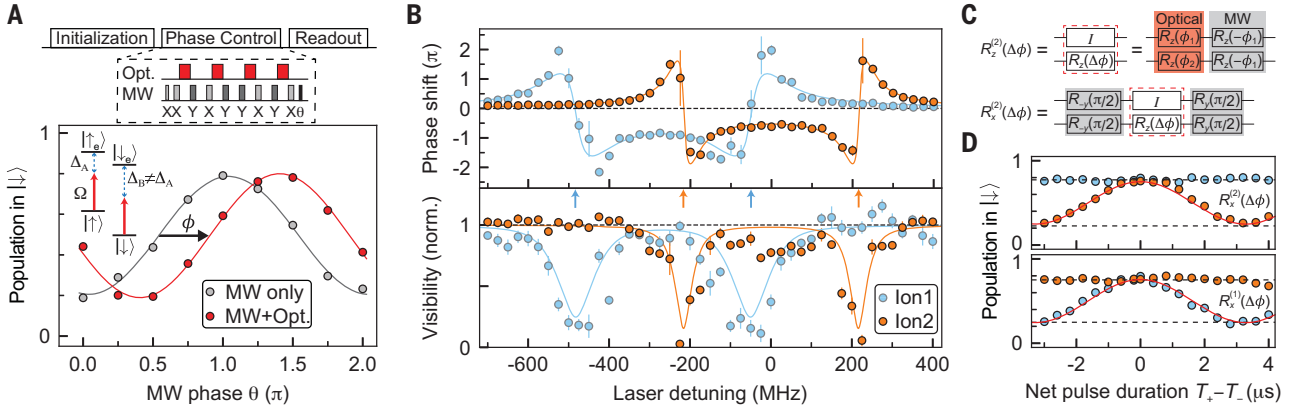

Fig. 3. Coherent optical spin rotation using the AC Stark shift. (**A**) (Upper) Optical phase shifts are generated by using a sequence of detuned optical pulses interleaved with a microwave-driven XY8 decoupling sequence. (Lower) The phase shift is detected by varying the phase of the final microwave $\pi/2$ pulse before measuring the spin population. The phase shift (ϕ) and visibility are extracted from a sinusoidal fit. (**B**) Frequency dependence of the phase shift and change in visibility for each ion after a 2-μs optical pulse. The solid lines are numerical simulations, including spectral diffusion. The arrows indicate the frequencies of the A, B transitions for each ion. (**C**) Circuit diagram for implementing $R_{z,x}^{(i)}(\Delta\phi)$ rotations. (**D**) Ion-selective Rabi oscillations $R_x^{(i)}(\Delta\phi)$. Positive (negative) phase shifts are generated by placing optical pulses after the odd- (even-) numbered π pulses in the XY8 sequence, with total duration T_+ (T_-) (the laser detuning is 275 MHz). The dashed lines show the loss of contrast from dephasing measured in the absence of any optical pulses; excess dephasing from the optical pulses is not observable.

would make the ion 4 Larmor frequency different, enabling spectral addressing of its microwave transition. In Fig. 4D, we show the initialization and single-shot measurement outcomes for all 16 four-spin states.

We have demonstrated simultaneous frequency-domain addressing of multiple Er^{3+} spins within a diffraction-limited volume, realizing a complete set of operations: initialization, coherent control, and single-shot spin measurement. This is a step toward two applications. First, combined with realistic improvements in optical and spin coherence enabling indistinguishable single-photon emission and long-term quantum memories [using host crystals with higher site symmetry (*27*) and lower nuclear spin content (*31*)], this work may lead to frequency-multiplexed quantum repeaters with substantially faster entanglement generation rates. Second, this approach enables probing and manipulating single defects within dense, strongly interacting ensembles. The creation of these ensembles is within reach by using ion implantation: $N \approx 20$ ions implanted into a $(30\ \text{nm})^3$ volume would have a typical separation of 11 nm, corresponding to a magnetic dipolar interaction strength of 1 MHz (given the large magnetic moment in Er^{3+}), faster than the decoherence rate of the ground-state spin with dynamical decoupling (*29*).

REFERENCES AND NOTES

1. D. D. Awschalom, L. C. Bassett, A. S. Dzurak, E. L. Hu, J. R. Petta, *Science* **339**, 1174–1179 (2013).
2. T. H. Taminiau, J. Cramer, T. van der Sar, V. V. Dobrovitski, R. Hanson, *Nat. Nanotechnol.* **9**, 171–176 (2014).
3. G. Waldherr *et al.*, *Nature* **506**, 204–207 (2014).
4. W. Pfaff *et al.*, *Science* **345**, 532–535 (2014).
5. S. Choi *et al.*, *Nature* **543**, 221–225 (2017).
6. P. C. Maurer *et al.*, *Nat. Phys.* **6**, 912–918 (2010).
7. P. Neumann *et al.*, *Nat. Phys.* **6**, 249–253 (2010).
8. F. Dolde *et al.*, *Nat. Phys.* **9**, 139–143 (2013).
9. M. Grinolds *et al.*, *Nat. Phys.* **7**, 687–692 (2011).
10. S. Kolkowitz, Q. P. Unterreithmeier, S. D. Bennett, M. D. Lukin, *Phys. Rev. Lett.* **109**, 137601 (2012).
11. T. H. Taminiau *et al.*, *Phys. Rev. Lett.* **109**, 137602 (2012).
12. N. Zhao *et al.*, *Nat. Nanotechnol.* **7**, 657–662 (2012).
13. C. Bradley *et al.*, *Phys. Rev. X* **9**, 031045 (2019).
14. M. Zhong *et al.*, *Nature* **517**, 177–180 (2015).

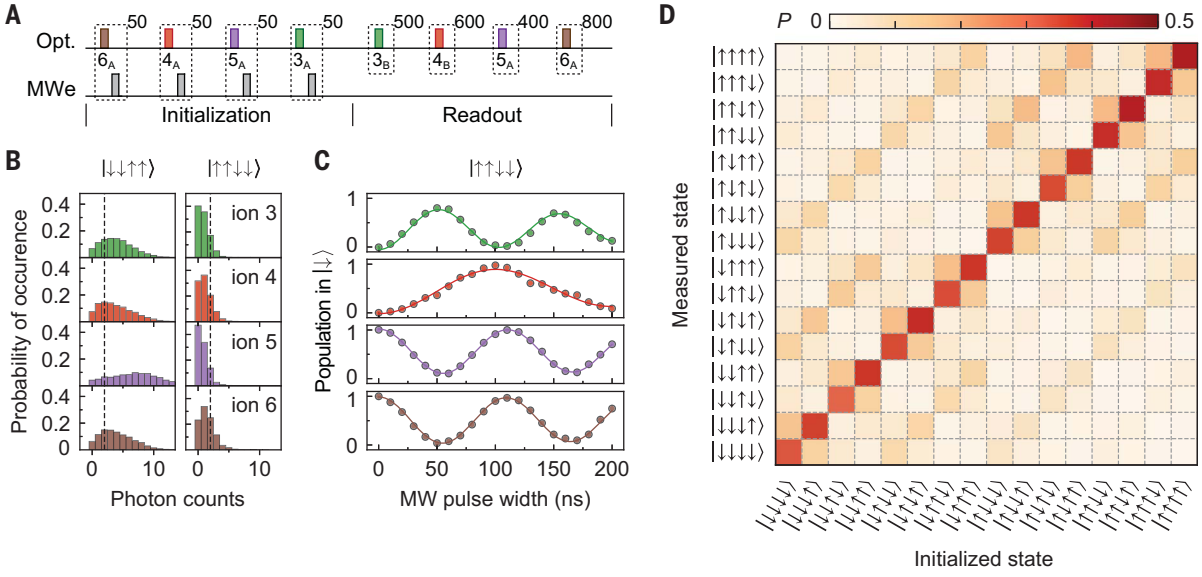

Fig. 4. Simultaneous initialization and readout of ions 3 to 6. (**A**) Pulse sequence for initialization and readout. (**B**) Histograms of detected photon counts for different initial states. The dashed lines indicate the threshold used for state discrimination. The spin state giving rise to higher counts depends on which transition is used for readout, which differs between ions. (**C**) Simultaneous microwave Rabi oscillations of all ions after being initialized to $|\uparrow\uparrow\downarrow\downarrow\rangle$. (**D**) Single-shot readout results for all 16 four-ion initial states. The average probability of obtaining the correct state for all four ions is $\bar{P} = 0.37$.

15. A. M. Dibos, M. Raha, C. M. Phenicie, J. D. Thompson, . *Phys. Rev. Lett.* **120**, 243601 (2018).
16. H. de Riedmatten, M. Afzelius, M. U. Staudt, C. Simon, N. Gisin, *Nature* **456**, 773–777 (2008).
17. E. Saglamyurek *et al*., *Nature* **469**, 512–515 (2011).
18. K. Ichimura, *Opt. Commun.* **196**, 119–125 (2001).
19. N. Ohlsson, R. Krishna Mohan, S. Kröll, *Opt. Commun.* **201**, 71–77 (2002).
20. J. H. Wesenberg, K. Mølmer, L. Rippe, S. Kröll, *Phys. Rev. A* **75**, 012304 (2007).
21. R. Ahlefeldt, M. Pearce, M. Hush, M. Sellars, *Phys. Rev. A* **101**, 012309 (2020).
22. G. J. Pryde, M. J. Sellars, N. B. Manson, *Phys. Rev. Lett.* **84**, 1152–1155 (2000).
23. J. Longdell, M. Sellars, *Phys. Rev. A* **69**, 032307 (2004).
24. J. J. Longdell, M. J. Sellars, N. B. Manson, *Phys. Rev. Lett.* **93**, 130503 (2004).
25. T. Zhong *et al*., *Phys. Rev. Lett.* **121**, 183603 (2018).
26. M. Raha *et al*., *Nat. Commun.* **11**, 1605 (2020).
27. J. M. Kindem *et al*., *Nature* **580**, 201–204 (2020).
28. M. Afzelius *et al*., *J. Lumin.* **130**, 1566–1571 (2010).
29. See the supplementary materials.
30. B. B. Buckley, G. D. Fuchs, L. C. Bassett, D. D. Awschalom, *Science* **330**, 1212–1215 (2010).
31. C. M. Phenicie *et al*., *Nano Lett.* **19**, 8928–8933 (2019).
32. S. Chen, M. Raha, C. M. Phenicie, S. Ourari, J. D. Thompson, Replication Data for: Parallel single-shot measurement and coherent control of solid-state spins below the diffraction limit, Harvard Dataverse, V1 (2020); https://doi.org/10.7910/DVN/5XMCMU.

ACKNOWLEDGMENTS

We gratefully acknowledge conversations with N. de Leon and M. Tuna Uysal. **Funding:** Support for this research was provided by the National Science Foundation (NSF, EFRI ACQUIRE program grant 1640959), the Princeton Center for Complex Materials (PCCM), an NSF MRSEC (DMR-1420541), the Air Force Office of Scientific Research (grant FA9550-18-1-0081), and the DARPA DRINQS program (grant D18AC00015). We acknowledge the use of Princeton's Imaging and Analysis Center, which is partially supported by the PCCM, as well as the Princeton Micro-Nano Fabrication Lab and Quantum Device Nanofabrication Lab facilities. C.M.P. was supported by the Department of Defense through the National Defense Science and Engineering Graduate Fellowship Program. **Author contributions:** S.C., M.R., C.M.P., S.O., and J.D.T. contributed to the design and execution of the experiment. S.C., M.R., and J.D.T. analyzed the data and wrote the manuscript. **Completing interests:** The authors declare no competing interests. **Data and materials availability:** All (other) data needed to evaluate the conclusions in the paper are present in the paper or the supplementary materials and are publicly available at Harvard Dataverse (*32*).

SUPPLEMENTARY MATERIALS

science.sciencemag.org/content/370/6516/592/suppl/DC1
Supplementary Text
Figs. S1 to S9
References (*33*, *34*)

13 May 2020; accepted 11 September 2020
10.1126/science.abc7821

Parallel single-shot measurement and coherent control of solid-state spins below the diffraction limit

Songtao ChenMouktik RahaChristopher M. PhenicieSalim OurariJeff D. Thompson

Science, 370 (6516), • DOI: 10.1126/science.abc7821

Addressing the many and the individual

The ability to coherently manipulate the quantum state of atomic defects in solid-state systems is a promising route to developing a platform for quantum technologies. A successful platform requires the interaction of many qubits in close proximity, as well as the ability to address each qubit individually, and, to date, such requirements have run counter to each other. Chen *et al.* devised an optical frequency-domain method with which they were able to simultaneously address many individual rare-earth ion defects (six at this point) with separations all within the diffraction limit of the control light. Because the approach is scalable to tens or hundreds of defects, it provides the prospect of realizing truly large-scale quantum processors.

Science, this issue p. 592